Structural and chemical modifications of oxides and OH generation by space weathering: Electron microscopic/spectroscopic study of hydrogen-ion-irradiated Al$_2$O$_3$

Yohei Igami [a,b,*], Shunsuke Muto [a], Aki Takigawa [c], Masahiro Ohtsuka [a], Akira Miyake [b], Kohtaku Suzuki [d], Keisuke Yasuda [e], Akira Tsuchiyama [f,g,h]

[a] *Institute of Materials and Systems for Sustainability, Nagoya University, Furo-cho, Chikusa-ku, Nagoya 464-8603, Japan*
[b] *Division of Earth and Planetary Sciences, Kyoto University, Kitashirakawa-Oiwakecho, Sakyo-ku, Kyoto 606-8502, Japan*
[c] *Department of Earth and Planetary Science, The University of Tokyo, 7-3-1 Hongo, Bunkyo-ku, Tokyo 113-0033, Japan*
[d] *The Wakasa Wan Energy Research Center, Tsuruga, Fukui 914-0192, Japan*
[e] *Graduate School of Life and Environmental Science, Kyoto Prefectural University, Shimogamo-Hangicho, Sakyo-ku, Kyoto 606-8522, Japan*
[f] *Research Organization of Science and Technology, Ritsumeikan University, Kusatsu 525-8577, Japan*
[g] *CAS Key Laboratory of Mineralogy and Metallogeny/Guangdong Provincial Key Laboratory of Mineral Physics and Materials, Guangzhou Institute of Geochemistry, Chinese Academy of Sciences, Guangzhou 510640, China*
[h] *CAS Center for Excellence in Deep Earth Science, Guangzhou 510640, China*

Abstract

Minerals on airless bodies exhibit characteristic spectral features such as darkening and reddening. Such space weathering is mainly due to hydrogen-ion irradiation by the solar wind and to micrometeorite impacts. Because of the reactivity of hydrogen, the associated H-implantation into O-bearing minerals can lead to the formation of new chemical bonds and may contribute to formation of water. However, laboratory studies still conflict about production efficiency of water and relevant H-bearing molecules such as OH formed by the H-ion irradiation. The production efficiency of the molecules within minerals may be influenced by short-range structural order of the host minerals. It is thus important to clarify how the implanted H interacts with various irradiation defects produced by H-ion bombardment. Here, we investigated H-ion-irradiated alumina (Al$_2$O$_3$), one of the most basic oxides, using scanning/transmission electron microscopy (S/TEM) and electron energy-loss spectroscopy (EELS). The TEM images revealed dense dislocations, nanoscale voids and nanoscale cracks—instead of amorphization—in the region subject to high energy deposition. Our analyses by STEM–EELS hyperspectral imaging (HSI) isolated a few essential spectral components, suggesting that chemical interactions between the implanted H and the host alumina resulted in local generation of OH species rather than amorphization. We also found a spectral feature which may be explained by H$_2$ gas, presumably remaining in the nanovoids, most of which escaped through fractures formed by the coalescence of the high-pressure H$_2$ nanobubbles. Such fractures/crack surfaces can act as additional reactive sites for the formation of the OH species. The present results strongly imply that H$^+$ irradiation can be a source of water in minerals

---

* Corresponding author at: Division of Earth and Planetary Sciences, Kyoto University, Kitashirakawa-Oiwakecho, Sakyo-ku, Kyoto 606-8502, Japan.

E-mail address: y-igami@kueps.kyoto-u.ac.jp (Y. Igami).

in various astrophysical conditions. The present methodology can be applied to a wide range of extraterrestrial materials, such as regolith grains, interplanetary-dust particles, and/or presolar grains in primitive meteorites.

1. INTRODUCTION

Minerals on the surfaces of airless bodies such as Moon and asteroids exhibit characteristic spectral features such as darkening and reddening due to space weathering (Pieters et al., 2000; Hapke, 2001; Clark et al., 2002). The main cause of space weathering is either bombardment of micrometeorites or irradiation of the solar wind. Detailed analyses of damaged textures on the actual regolith grains—brought back directly from airless bodies such as Moon and the asteroid Itokawa—suggest that solar-wind irradiation, ~95% of which is attributable to hydrogen (H) ions (Reisenfeld et al., 2003, 2007), should be responsible for their characteristic textures (Dran et al., 1970; Christoffersen et al., 1996; Keller and McKay, 1997; Noguchi et al., 2011, 2014; Pieters and Noble, 2016). In addition, damaged rims produced by the solar wind irradiation were also found in crystalline silicates from chondritic porous interplanetary-dust particles (CP-IDPs; Bradley et al., 2014). Similar interactions between energetic H ions and solids can occur in various other astrophysical environments as well. Infrared spectroscopic observations have shown that crystalline dust is almost absent in the interstellar medium (ISM) (Kemper et al., 2004, 2005). It has been proposed that the low crystallinity of dust in the ISM may be caused by collisions between dust and low-energy (<1 MeV) ionized gas species, which mainly consist of H^+ accelerated by supernova shockwaves (Day, 1977; Jones et al., 1996; Demyk et al., 2001, 2004; Carrez et al., 2002; Jäger et al., 2003; Kemper et al., 2004, 2005,). Some of GEMS (glass with embedded metal and sulfides) particles in IDPs might be produced by amorphization of crystalline circumstellar dust by ion irradiation in the ISM (Bradley and Dai, 2004; Bradley, 2013). In this paper, we refer to such destruction of interstellar dust due to ion irradiation also as 'space weathering' in a broad sense.

The interaction between energetic H^+ and minerals containing oxygen as a primary constituent element has the potential to produce a significant amount of water within grains. The M^3 mission to the Moon (the Moon Mineralogy Mapper aboard *Chandrayaan-1*) revealed that H_2O/OH is present on the Moon at all latitudes (Pieters et al., 2009; Li and Milliken 2017; Li et al., 2018; Bandfield et al., 2018), and data returned by several other spacecraft have shown consistent results (Sunshine et al., 2009; Clark 2009). This strongly implies that the H^+ originating continuously from the solar wind has contributed significantly to the production of water on the Moon. The solar-wind irradiation to protoplanetary dust or planetesimals might also generate OH/H_2O species even in anhydrous minerals. Accretion of such protoplanetary dust or planetesimals had possibly supplied water to the proto-Earth as well as the accretion of carbonaceous chondrites and comets as late-veneer.

To understand the efficiency of production of water by H-ion irradiation, laboratory/experimental studies have explored various minerals. Several studies found OH/H_2O absorption lines in infrared spectra of H-ion-irradiated silicates (Zeller et al., 1966; Ichimura et al., 2012; Nakauchi et al., 2021), and the H_2O/OH signature was detected also by secondary-ion mass spectrometry (Managadze et al., 2011). In contrast, Burke et al. (2011) used the same analytical methods and reported no evidence for H_2O/OH in silicate or oxide. There are attempts to detect H more directly in nanometer scale using scanning transmission electron microscopy (STEM) accompanied by electron energy-loss spectroscopy (EELS). Bradley et al. (2014) and Zhu et al. (2019) showed unambiguous evidence for H_2O/OH in low-loss spectra from silicates in CP-IDPs or their experimental analogs, whereas Burgess and Stroud (2018) reported no clear evidence for the presence of H from lunar oxides, although they found a significant He-K edge in their low-loss spectra.

The production and survival probability of H-bearing species in minerals are expected to be influenced by short-range structural modifications in the host minerals produced by H-ion bombardment. STEM–EELS has the potential not only to characterize the local atomic structure but also to determine the chemical states of the target materials at the nanometer scale. Here, we report the results of STEM–EELS analyses for an experimentally H-ion-irradiated mineral. We used α-alumina (corundum, Al_2O_3), one of the most basic model oxides, as the target mineral for the present experiments, which we intend as a first step toward understanding the elementary process of space weathering caused by H-ion irradiation. In addition, we applied a multivariate spectral-resolution technique to the hyperspectral-imaging (HSI) dataset, which is a set of spectroscopic data sampled with a small step width by scanning an electron probe over the specified region of interest to extract the underlying chemical components and their spatial abundance maps (Muto & Shiga, 2020).

2. EXPERIMENTAL PROCEDURE

2.1. Sample

We removed the surface-damage layer produced by mechanical polishing of a single-crystal alumina plate chemically using colloidal silica and then cut it into $\sim 3 \times 3 \times 0.5$ mm^3 pieces. We performed the irradiation experiments using a 200 kV ion-implanter at the Wakasa Wan Energy Research Center (Hatori et al., 2005, 2021). The sample was irradiated with 40 keV H_2^+ ions. During

the irradiation, the temperature of the sample was kept at ~30 °C by water-cooling. A small molecular ion is generally dissociated by impact at the solid surface and penetrates independently as two atoms within the sample (e.g., Sigmund et al., 1996; Arista, 2000; Wieser et al., 2002; Burke et al., 2011). The present irradiation flux of the 40 keV H_2^+ ions was ~8×10^{13} ions cm^{-2} sec^{-1}, and the total dose was ~1×10^{18} ions cm^{-2}, which is equivalent to irradiation of 20 keV H^+ ions with the dose of ~2×10^{18} ions cm^{-2}. For comparison, the solar-wind flux at ~1 AU is ~2×10^8 ions cm^{-2} sec^{-1} (Goldstein et al., 1996; Heber et al., 2012). These flux values are low enough to allow us to ignore the effects of multiple ion interactions, because the time interval between two subsequent H^+ impacts within an area of ~10^2 nm^2 is estimated to be ~10^{-2} s for the laboratory experiment and ~5×10^3 s for the solar wind. Both are long enough to allow multiple ion interactions to be ignored, because the typical excitation volume associated with an atomic-collision cascade ranges over ~10 nm, which relaxes and cools down to the ground state in ~10^{-11} s (Ishino, 1993). We thus consider space weathering to be built up by independent processes of subsequent single-ion injection events into the alumina. Fig. 1 shows the distributions of the number of displacements of Al and O atoms by elastic collisions and the implanted H abundance for the present experiment, as simulated by the SRIM code, which is based on the Monte Carlo method
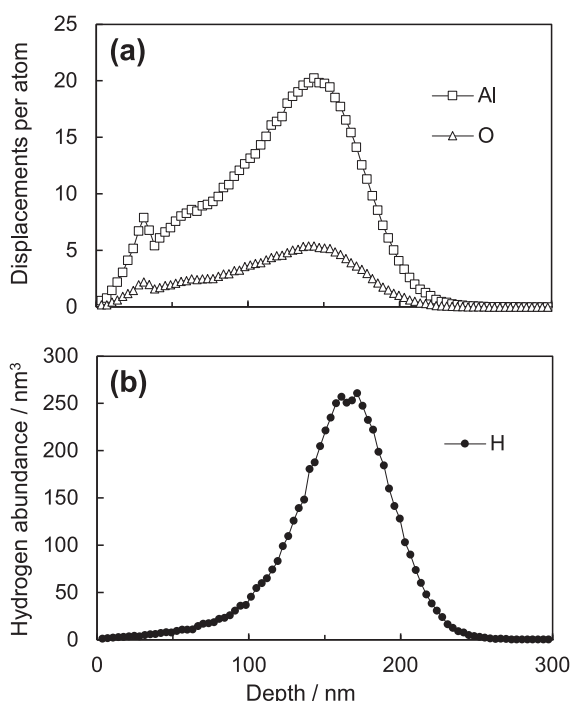
(Ziegler et al., 1985, 2013), with displacement energies of 20 eV for Al and 50 eV for O (Zinkle and Kinoshita, 1997).

2.2. Preparation for TEM analysis

For the TEM analyses, we prepared a cross-sectional thin section perpendicular to the irradiation surface from the irradiated sample, using a focused ion beam with scanning electron microscope (FIB-SEM) system Helios Nano-Lab G3 CX (Thermo Fisher Scientific). Over the entire irradiated surface of the sample, relatively flat blisters (~3 μm in diameter) and exfoliation textures were observed by SEM (Fig. 2). We extracted a cross-sectioned piece including an exfoliated blister using an *in-situ* tungsten probe and mounted it on a TEM grid. Before the extraction, we coated the sample surfaces with an electron-beam-deposited Pt layer at 5 kV (~100 nm in thickness), followed by a Ga$^+$-beam-deposited Pt layer at 30 kV (~1 μm in thickness). Final thinning down to a thickness of 100–150 nm was done using 30 kV Ga$^+$ ions, with beam currents in the range 0.1–1 nA, to prevent conceivable gas species such as H_2 or H_2O from dissipating from the specimen. We followed this by removing the surface-damage layer using 5 kV Ga$^+$ ions with a beam current of ~20 pA.

2.3. TEM and STEM–EELS analyses

We obtained bright-field and dark-field (BF/DF) TEM images and selected-area electron-diffraction (SAED) patterns using a JEM-2100 TEM (JEOL) operated at 200 kV, equipped with a side-mounted CCD camera ES500W Erlangshen (Gatan). Since the FIB-fabricated sample was relatively too thick to allow successful EELS analysis using a conventional 200 kV-class TEM, we used a JEM-1000 K RS ultra-high-voltage TEM (JEOL) operated at 1000 kV,

Fig. 1. Depth distributions of displacement damage and implanted H, as calculated by the SRIM code (Ziegler et al., 2013) for an H$^+$ dose of 2×10^{18} ions/cm^2 (the present experimental condition). (a) Depth distributions of number of displacements of Al and O atoms by elastic collisions. (b) Depth distributions of number of implanted H atoms. The small peaks at the depth of ~30 nm are ascribed to numerical error and have no physical meaning.
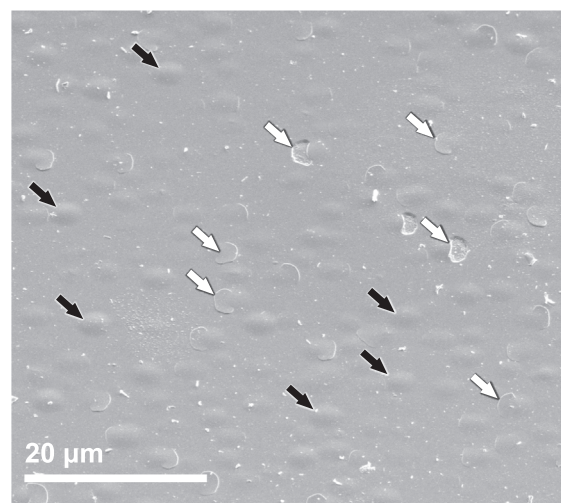

Fig. 2. Secondary electron image of the surface of the irradiated alumina sample. Incident angle of the electron beam is 45° relative to the surface normal. Relatively flat blisters (~3 μm in diameter) and exfoliation textures are observed over the entire irradiated surface. Some of the flat blisters and exfoliation textures are indicated using the black and white arrows, respectively.

equipped with a Gatan Image Filter (GIF) Quantum-equivalent post-column EELS detector (Gatan) to obtain better TEM images and STEM–EELS hyperspectral-imaging (HSI) data. The EELS–HSI datasets were acquired using an electron probe with a diameter of ~2 nm, current density of ~10 pA/nm^2 and a zero-loss peak (ZLP) energy resolution (FWHM) of ~1.5–2.0 eV, from the low-loss region (~0–180 eV) that includes the H-K and Al-L$_{2,3}$ edges using a step width of 4.7 nm and acquisition time of 0.001 sec/step, and from the region for the O-K edge (~480–610 eV) using a step width of 11.7 nm and acquisition time of 10 sec/step, both with an energy dispersion of 0.1 eV/channel.

2.4. Nonnegative matrix factorization (NMF) analysis of EELS–HSI datasets

Fine structures in EEL spectra are sensitively changed by slight modifications in chemical state and/or local structure. However, such different spectral profiles can overlap in spatially overlapping regions. This problem can be reasonably resolved by statistically extracting a few basic-component spectra from a STEM–EELS–HSI dataset assuming that the spectral intensity at each sampling point is represented by a linear combination of the few component spectra associated with the underlying chemical states. Such problems are popularly solved through principal component analysis (Bonnet et al., 1999; Trebbia and Bonnet, 1990; Bosman et al., 2006), but this fundamental approach usually provides physically meaningless spectra with negative values. An alternative and promising method is NMF, which finds a solution under the nonnegativity restriction of both the component spectra and their spatial distributions. NMF and its improvements have successfully separated the overlapped spectral fine features in EELS–HSI datasets (e.g., Muto and Tatsumi, 2017; Muto and Shiga, 2020).

In this study, all the obtained EELS–HSI datasets were analyzed using NMF to isolate the underlying spectral components and visualize their spatial distributions. The number of components was carefully determined in each dataset by NMF trials starting with two components and increasing the number of components until some components show physically meaningless spectra or spatial distributions. Although NMF solutions may not always coincide with the true solutions, the obtained low-rank representations are easily discussed and are physically, chemically, mineralogically and planetologically more interpretable than raw datasets comprising many noisy spectra. Based on previous EELS measurements and the first-principles calculations of the density of state (DOS) of relevant phases, we carefully interpreted the fine structures in the NMF-processed EEL spectra (Ahn et al., 1983; Muto et al., 2009; Jiang and Spence, 2011).

3. RESULTS

3.1. TEM observations

Fig. 3 shows a low-magnification TEM image in the vicinity of the irradiation surface of the specimen. An exfo-
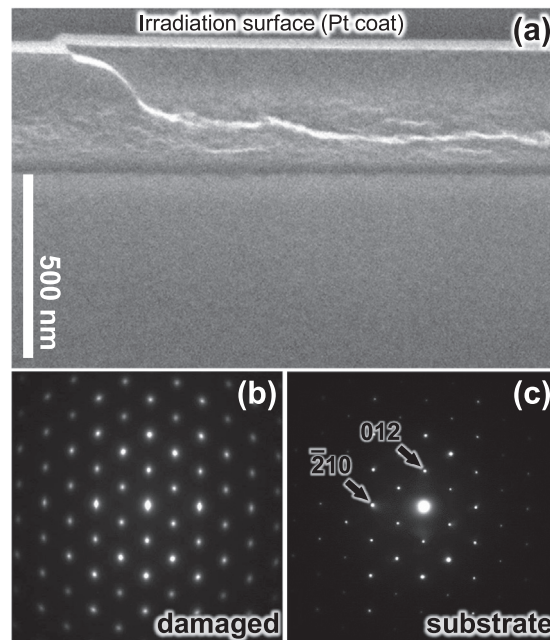

Fig. 3. 200-kV TEM image and SAED patterns of a cross-sectional specimen. (a) Low-magnification TEM image in the vicinity of the irradiation surface of the specimen. The damaged layer extends from the surface down to a depth of ~300 nm. (b) SAED pattern taken from the damage region and (c) SAED pattern from the substrate.

liation texture at an edge of a flat blister is observed. The damaged layer extends from the surface down to a depth of ~300 nm, which corresponds approximately to the region around the damage peak in the SRIM simulation (Fig. 1), although the two do not completely match due to swelling effect of the damage layer that is not simulated in the SRIM calculation. In the damaged region, we observed a pile of nanocracks roughly parallel to the surface (Fig. 3a). The largest crack propagates to the surface to form the exfoliation texture. Fig. 3b and 3c show SAED patterns taken from the damaged region and substrate region, respectively (the selected regions are ~220 nm in diameter). The geometry of the SAED pattern from the damaged region (Fig. 3b) is identified as the $[1\,\bar{2}\,1]$ zone of α-alumina (Fig. 3c), which is the same as that from the substrate. The diffraction spots are slightly elongated perpendicular to the surface, suggesting fragmentation of the structure along this direction. No extra spots due to formation of additional crystalline phases were observed.

Fig. 4 shows enlarged BF and DF TEM images of a part of the damaged region obtained through the 1000-kV TEM. Dense dislocations are present throughout the damaged region, as shown clearly in the DF image (Fig. 4b). Alumina is not fully amorphized, even in the region of the damage peak where the damage is larger than 1 dpa (displacement per atom) (a standard criterion for amorphization), as shown in Fig. 1. This is unlike most silicates (e.g., Carrez et al., 2002; Jäger et al., 2003; Demyk et al., 2004; Thompson et al., 2014; Matsumoto et al., 2015). Damaged rims without amorphization were observed on
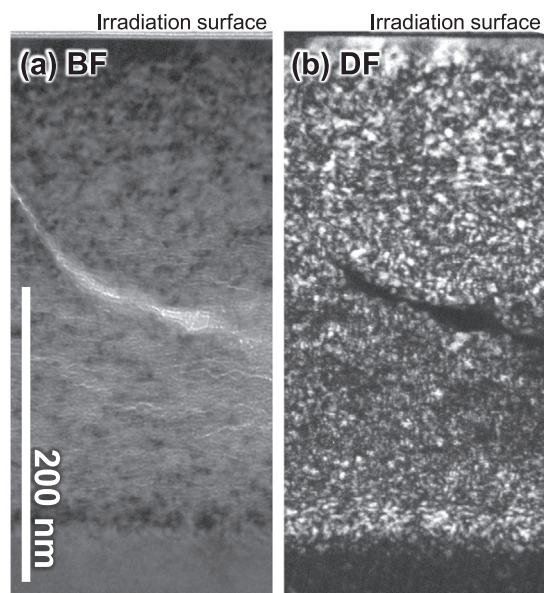
Fig. 4. 1000-kV TEM images of the damaged region projected onto the [1 2 1] zone axis of α-alumina. (a) BF-TEM image. (b) DF-TEM image taken with the 024 reflection. Note that the damaged region is not amorphized.

olivine regolith grains from Itokawa, but these rims might be generated by irradiation and subsequent heating and recrystallization of amorphous rims (Harries and Langenhorst, 2014).

Fig. 5 shows 1000-kV TEM images of the damaged region imaged under different defocused conditions to enable better understanding of the structures associated with the dot-shaped objects (arrows). These objects can be identified as nanovoids, rather than dislocations or metallic precipitates, because their contrast inverts from bright to dark as the focus is changed from under-focused to over-focused, which is typical of a Fresnel fringe at a sharp edge. The voids are roughly 1 nm in diameter (Fig. 5c–d), which is similar to the sizes observed in previous studies of ion irradiated ceramic materials such as alumina and spinel (e.g., Zinkle, 2012). They do not have the planar or faceted shapes, which are frequently observed in irradiated samples experienced in some heating events (Zinkle, 2012; Christoffersen et al., 1996; Burgess and Stroud, 2018). The voids are more densely distributed independently of crystallographic planes, particularly over the depth between ~100 and 300 nm below the surface (Fig. 5a–b), consistent with the H distribution predicted by the SRIM profile (Fig. 1). This strongly suggests that a significant number of H atoms have aggregated to form H_2 bubbles near the end of their trajectories within the alumina structure. In addition, in the region of the highest void concentration—around a depth of ~250 nm—some voids have coalesced in the direction approximately parallel to the surface. Void coalescence thus likely triggers the formation of nanocracks, which eventually develop into the observed exfoliation and the heavily damaged textures.

3.2. Al-$L_{2,3}$ and O-K core-loss spectra

We obtained the STEM–EELS–HSI datasets from the region enclosed by the dashed and dotted rectangular insets in Fig. 6(a). Representative spectra extracted from some regions such as substrate and damaged region in the datasets are shown in Figs. S1 and S2. Fig. 6(b)–(g) summarize the results of two-component analyses obtained by applying NMF to the HSI dataset for the Al-$L_{2,3}$ (Fig. 6b–d) and that for the O-K (Fig. 6e–g), showing the resolved spectral endmembers and their respective abundance maps.

Comp-A1 and Comp-O1 (the first components of the Al-$L_{2,3}$ and O-K) corresponds to the original material, α-alumina, judging from its spectral profile (e.g., Muto et al., 2009; Ahn et al., 1983). They are widely distributed with high concentration excluding nanocrack region. The second component of the Al-$L_{2,3}$, Comp-A2, can be interpreted from its lower-energy spectral onset and spectral fine structure to be due to metallic Al, $Al(OH)_3$, AlH_3, or combinations of these species (Muto et al., 2009; Jiang and Spence, 2011), rather than to possible oxide phases such as α, γ, or amorphous alumina. This suggests that Comp-A2 can be attributed to the deoxidization of Al and/or the hydroxylation of O. The spatial distribution of Comp-A2 is highly localized over the nanocrack region where Comp-A1 shows low concentration. The second component of the O-K spectrum, Comp-O2, shows a broad main peak extending to the lower-energy-loss side, with a characteristic small pre-edge peak (the arrow in Fig. 6g). These features coincide well with those from electron-irradiated Al$(OH)_3$, as reported by Jiang and Spence (2011), among the other possible phases available in the Al–O–H system. Note that Comp-O2 is also localized in the nanocrack region like Comp-A2. Comp-O2 seems slightly more extended beyond the nanocrack distribution than Comp-A2, but this may arise from the difference in the step width for the EELS collection.

3.3. Plasmon loss spectra

We also obtained a low-loss HSI dataset from the same region as in Fig. 6a. Representative spectra extracted from some regions such as substrate and damaged region in the dataset are shown in Fig. S3. Fig. 7 summarizes the results of a three-component NMF analysis, applied to the data after removing ZLP. Fig. 7a–c show abundance maps of Comp-L1, Comp-L2, and Comp-L3, and Fig. 7d shows the corresponding endmember spectra.

Comp-L1 can be identified from the component spectrum showing a peak at ~25 eV and its high concentration—which is distributed widely over the entire depth, including the substrate (Fig. 7a)—to be the original α-alumina. The small feature at ~15 eV (indicated by the arrow in Fig. 7d) is commonly detected in the substrate region and in non-irradiated α-alumina in previous reports (e.g., French et al., 1998). This feature may be due to some interband transition or surface plasmon, which is roughly estimated as ~18 eV from the volume plasmon energy divided by $\sqrt{2}$ (Egerton, 1978), and due to the volume plasmon of metallic Al (~15 eV, Ahn et al., 1983) which may
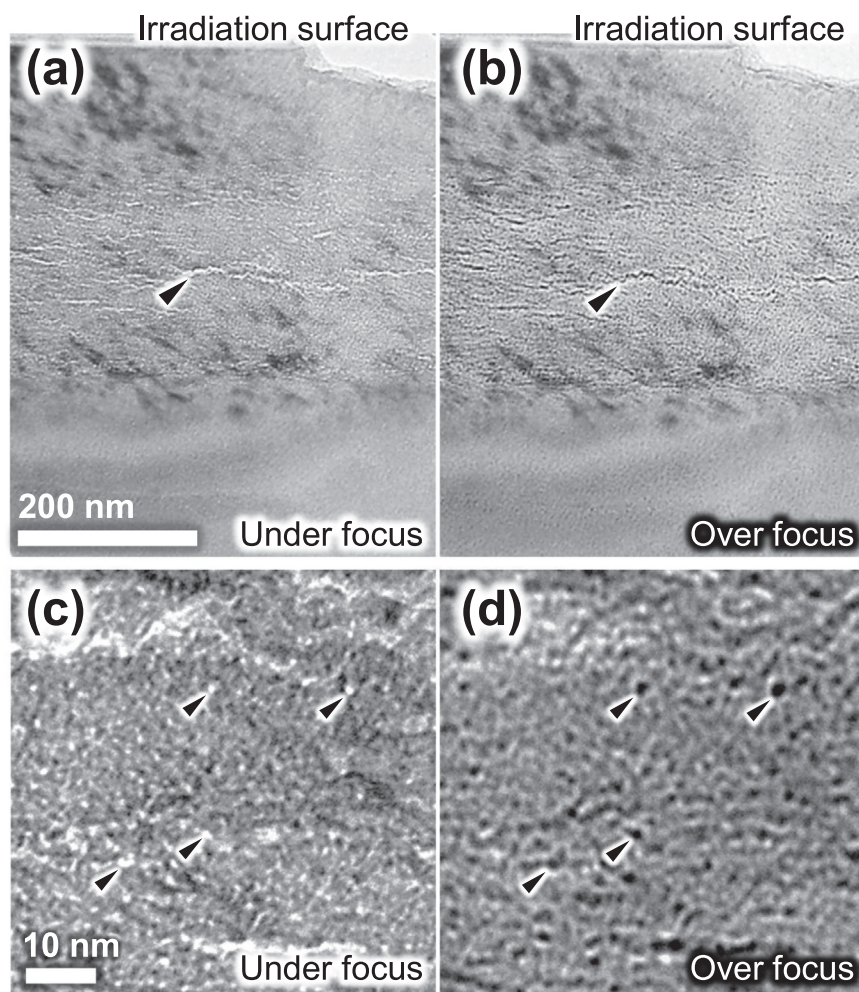
Fig. 5. 1000-kV TEM images of the damaged region taken at under-focused (a, c) and over-focused (b, d) conditions. Nanovoids with diameters of ~1 nm are visible as bright and dark contrasts in the under-focused and over-focused conditions, respectively (indicated by arrows).

have been caused by Ga^+-ion irradiation during FIB processing and/or electron-beam irradiation in TEM.

Comp-L2 is highly localized around a depth of ~250 nm, adjacent to the nanocrack region (Figs. 4 and 6a). The component spectrum shows a peak at ~21 eV, suggesting a lower-density phase like an amorphous alumina film (Perevalov et al., 2010). Comp-L2 is thus likely to be a highly defective state of alumina.

Comp-L3 is relatively extended over a wide range of depths around 100–300 nm in the damaged region. The component spectrum of Comp-L3 shows a main peak at ~23 eV, about 1.5 eV lower than that of Comp-L1. The plasmon energy E_p is expressed by the following equation, based on the free-electron–gas model (i.e., the Drude model, Drude, 1900):

$$E_p = \frac{h}{2\pi} \sqrt{\frac{ne^2}{m_e \varepsilon_0}} \propto \sqrt{n}, \tag{1}$$

where h is Planck's constant, n is the valence-electron density, e is the electron charge, m_e is the electron mass, and ε_0

is the dielectric constant of the vacuum. If the lower peak energy of Comp-L3 were to be ascribed solely to the volume change with no compositional change, more than a 10% volume expansion would be required. Previous neutron-irradiation experiments found only ~4% volume expansion, even for ~20 dpa damage (Pells, 1994). This strongly suggests that some chemical modifications are necessary to explain the peak shift of Comp-L3. The formation of Al(OH)$_3$ provides a possible and reasonable explanation for this, since peak position of plasmon of Al(OH)$_3$ is comparable (Jiang and Spence, 2011) and the existence of OH is consistent with the Comp-O2 feature discussed in the previous section. In time-dependent EELS acquisition and DOS calculations, Jiang and Spence (2011) showed a fine feature of Al(OH)$_3$ around 9.1 eV, but it was easily destroyed by H depletion under electron-beam irradiation. The depletion of H in Al(OH)$_3$ is reasonable also to explain the O-K spectrum in the present measurements because according to Jiang and Spence (2011), pre-edge peak, such as that shown in Fig. 6g, are not an intrinsic feature of Al(OH)$_3$ but are
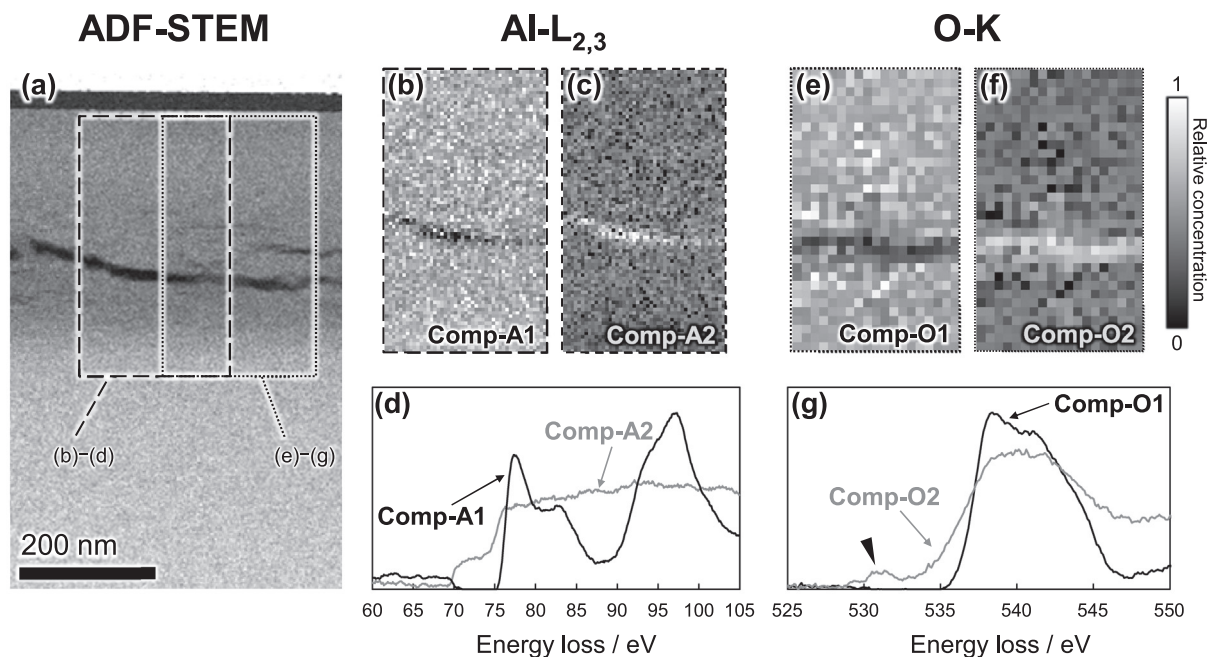
Fig. 6. Annular dark-field STEM image around the damaged region (a) and the results of two-component NMF analyses for the HSI dataset from this region for the Al-$L_{2,3}$ edge (b–d) and for the O-K edge (e–g), showing abundance maps (b–c and e–f) and endmember spectra (d and g).
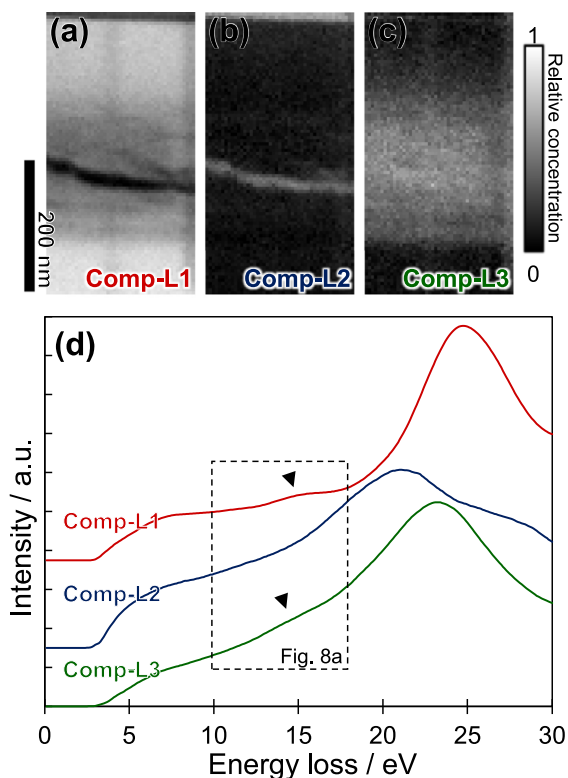

Fig. 7. Results of three-component NMF analysis for the low-loss HSI dataset. (a–c) Abundance maps of Comp-L1, Comp-L2, and Comp-L3. (d) The corresponding spectral endmembers.

generated only after H depletion. In summary, hydroxylation likely occurred, resulting in the relatively broad distribution interacting with collisional defects in the damaged region. The spectral features related to OH species may be influenced also by the surface adsorption of some molecules such as atmospheric water that is spatially uniform on the thin-section surface.

3.4. Fine features in low-loss spectra and exploring H-bearing fluids

Let us focus on the characteristic spectral features around 15 eV in Comp-L1 and L3 (in the dashed rectangular inset in Fig. 7d), which are highlighted in Fig. 8a. We extracted the small features by subtracting a baseline (the dash-dotted lines in Fig. 8a), which we interpolated using spline fits to both energy sides of these features, as shown in Fig. 8b–c. The feature extracted from Comp-L1 was well fitted by a single Gaussian (Fig. 8b, gray line). On the other hand, the broad peak of Comp-L3 required two Gaussians (Fig. 8c, gray lines). The FWHM of the fitted Gaussian profiles are 1.6–2.7 eV, which is reasonable for detectable signals considering the present energy resolution of ZLP (FWHM is ~1.5–2.0 eV). The common peak at ~15 eV in Fig. 8b and c can be interpreted as some valence-electron excitation of alumina or being due to metallic Al (Fig. 8d), as already discussed above. The remaining peak located at lower energy, ~13.7 eV, may recall some localized surface plasmon resonance on the nanovoids, but the broad size variation of nanovoids (shown in Fig. 5) is unlikely the origin of the well-defined single peak. There is another possibility that the ~13.7 eV feature is ascribed
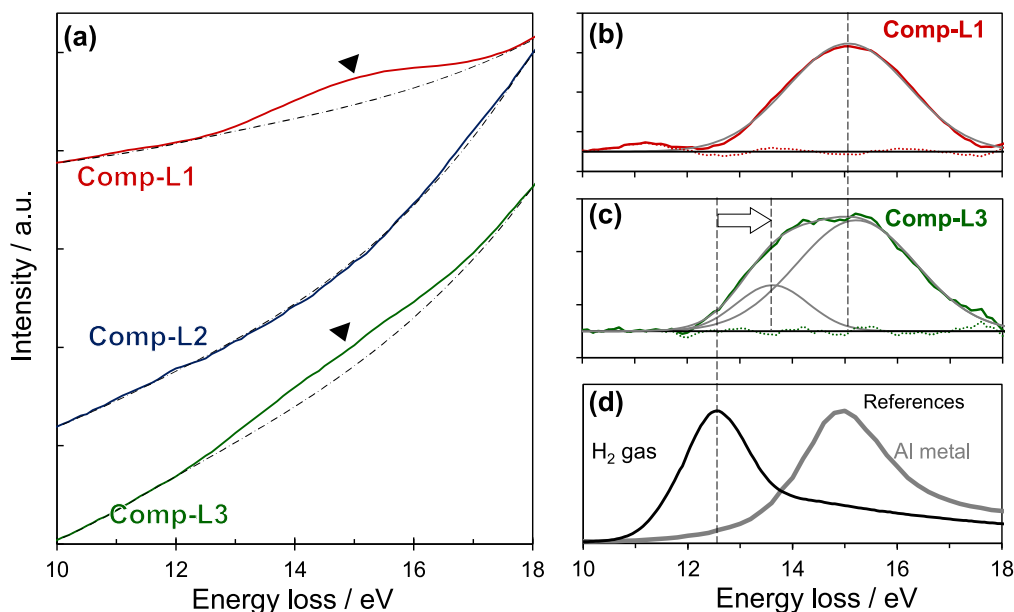
Fig. 8. (a) Enlargement of the lower-energy side of the plasmon peaks for Comp-L1–3, with baselines provided by the spline fits shown by the dash-dotted lines. (b–c) Gaussian fits to the features extracted respectively from Comp-L1 and 3 in (a). (d) Reference spectra reported for the H-K edge of H_2 gas and for the volume plasmon of metallic Al for comparison. See text for details.

to the H–K edge of H_2 gas, which is likely to have been incorporated into the nanovoids. The distribution of nanovoids visualized by the TEM imaging (Fig. 5a–b) is actually well correlated with the abundance map of Comp-L3 (Fig. 7c). Note that the peak is located at a slightly higher energy than those in the reference spectra (Fig. 7g). This is reasonable for H_2 bubbles, because the H_2 gas in the nanovoids is expected to be present at high pressure. Such a blue shift can be interpreted in terms of Pauli's exclusion principle for the 2p electron orbital excited from the 1s state of the neighboring atoms at high pressures (Rife et al., 1981); this has been applied in particular to He nanobubbles (Walsh et al., 2000; Fréchard et al., 2009; Taverna et al., 2008; Ono et al., 2019). A peak shift for an H_2 bubble has also been reported (Leapman and Sun, 1995).

Quantifying the possibly remaining H_2 gas is difficult because alumina with abundant nanovoids may contribute to slight modifications in the low-loss spectra as discussed before. However, we can discuss about the maximum amount of the remaining H_2. Assuming that the ~13.7 eV feature observed in our spectra is ascribed to H-K edge alone, the maximum projected number density of H can be estimated from the EEL spectral intensities using the following equation:

$$N_H = \frac{I_H}{I_0 \sigma_H} \tag{2}$$

where I_H is the intensity of the H-K edge, I_0 is the zero-loss intensity, and σ_H is the cross-section for the 1s–2p transition of H (Egerton, 1978). From our HSI data, I_H was determined using the Gaussian peak area of H-K edge in Comp-L3 spectrum (as shown in Fig. 8c). This yields a rough estimate of the projected number density of H, N_H ~140 H/nm^2, in the high-concentration region of Comp-

L3 (~150–250 nm in depth). If the average sample thickness of this region is assumed to be ~150 nm, the number density of H can be estimated to be ~1 H/nm^3 at most. This corresponds to ~0.5% of the amount of H atoms implanted around this region, as predicted by the SRIM simulations (Fig. 1). This implies that most of the H_2 gas present in the alumina escaped through the leakage paths generated by the coalescence of the nanovoids.

4. DISCUSSION

4.1. Effects of implanted hydrogen in the alteration of alumina

The present results suggest that the implanted H atoms are chemically trapped near the end of their trajectories by being bonded mainly with O to generate ─OH species, effectively terminating the broken bonds. This is consistent with previous experiments, such as a report by Sasajima et al. (1999), which found by TEM observation that the defect size due to H^+ irradiation was significantly larger than that formed by He^+ or O^+ irradiation, even when the displacement damage caused by H^+ was much smaller. On the other hand, the long-range order of α-alumina was not completely lost, even at a damage of >1 dpa. As the damage and local H concentration increase, fine gaps or clusters of vacancies develop with their broken bonds H-terminated, wherein further incoming H can be trapped (absorbed) and form H_2 molecules. Nanobubbles thus grow almost without volume expansion or diffusion until the internal H_2 pressure reaches the fracture limit of alumina. The observed nanocracks, which are approximately parallel to the irradiated surface, are likely formed by the coalescence of such neighboring nanobubbles at the peak implan-

tation depth of H (as shown in Fig. 1, Fig. 4a and b). This is eventually followed by exfoliation when the crack concentration increases beyond the percolation limit, producing escape paths for the H_2 gas out of the material. The newly formed fracture surfaces can again act as highly reactive sites to trap further H atoms and generate additional OH species. We thus conclude from the present results that in space weathering, the implanted H interacts with host minerals both chemically and mechanically.

4.2. Dependence of the production of H-bearing molecules on mineral species

The amount of H detected in the H-ion-irradiated minerals seems to correlate well with damage state of the host minerals. Burgess and Stroud (2018) performed STEM–EELS analyses for the solar-wind-irradiated oxide minerals ilmenite ($FeTiO_3$, a cation-ordered corundum structure) and Al-bearing chromite ($FeCr_2O_4$, a spinel structure) from the lunar regolith which retained their crystalline order, and they reported that there was no clear evidence for the presence of H, although they found significant He-K edges in their low-loss spectra. On the other hand, Bradley et al. (2014) analyzed fully amorphized rim on solar-wind-irradiated silicates (pyroxene) in CP-IDPs, and they found OH and H_2O with a detected amount of OH that is significantly larger than that in our specimen. Damage resistance of each mineral species to H-ion irradiation may be important for the production and/or retention of the H-bearing molecules within minerals.

In general, typical oxides require extremely high irradiation dose amounts for amorphization (White et al., 1989; Hobbs et al., 1994), while most silicates are much easier to be amorphized (e.g., Carrez et al., 2002; Jäger et al., 2003; Demyk et al., 2004) probably because the SiO_4 units and their networks, which form the basic frameworks of the silicates, are efficiently damaged by electron excitation (radiolysis) as well as by collisional events (Hobbs and Pascucci, 1980; Hobbs 1994). In more detail, the damage resistance to H-ion irradiation should be also attributed to several other chemical/physical properties of target minerals, such as chemical affinity with H and mechanical strength against local strains associated with irradiation-induced defects (e.g., White et al., 1989; Hobbs et al., 1994). More systematic studies are required to understand adequately the origin of the differences in the damaging/amorphization processes among various minerals, which may affect the production and retention rate of the H-bearing molecules.

4.3. Implications for space and planetary sciences

The irradiation dose amount of H ions in this study is approximately equivalent to that at 1 AU for ~100 years, adopting the H^+ flux of the solar wind to be $\sim 2 \times 10^8$ ions cm^{-2} sec^{-1} (Goldstein et al., 1996; Heber et al., 2012). Because the energy of solar wind H^+ ions is ~1 keV, implantation of the solar wind H^+ ions damages much smaller volume than that in the present study. Even if an amount of OH generated by solar-wind-irradiation is small,

regolith activities such as grain abrasion, fracturing, and/or grain motions (Matsumoto et al., 2016) provide fresh surfaces for continuous OH production on the asteroids. Moreover, the surface of airless bodies is mainly composed of silicates, which may be more capable of retaining OH-bearing defects than typical oxides for the reason given in Section 4.2.

Considering space weathering of interstellar dust, it is estimated that H^+-irradiation dose amount for grains with diameters $> \sim 250$ nm by a single supernova shock is $\sim 10^{18}$ ions/cm^2 on (Jones et al., 1996). Based on the present experiment, each dust grain may retain H_2 nanobubbles and OH species everywhere inside the grain, although most of the H_2 gas may escape soon after the formation through leakage paths generated by coalescence of the nanobubbles. The H^+-irradiated oxide/silicate dust particles can thus act as containers of OH/H_2O with relatively high heat resistance, unlike the previous assumption that H-bearing molecules are generated and adsorbed only on the surfaces of silicate/oxide dust particles (Vidali 2013).

Corundum (α-alumina) dust is observed in outflows from many evolved stars (Zeidler et al., 2013; Takigawa et al., 2014), and also has been discovered as presolar grains in some primitive meteorites, which are survivors of interstellar dust particles (e.g., Hutcheon et al., 1994; Nittler et al., 1997, 2008; Takigawa et al., 2014, 2018). Our study suggests that alumina irradiated by H^+ ions rigidly retains OH-bearing defects and a nanovoid texture without amorphization. The characteristic nanovoid texture can serve as a tracer to prove the presolar origin of a grain definitively if the nanovoids extend widely to the regions much deeper than ~50 nm from the surface where solar-wind H cannot arrive. The present high-voltage STEM–EELS with HSI–NMF technique is also applicable to future analyses of presolar alumina, which we expect to contribute to new discoveries related to presolar H-bearing molecules.

5. CONCLUSION

We have examined H-ion-irradiated alumina as a model sample in order to gain understanding of the detailed mechanism of space weathering due to H-ion irradiation by the solar wind and its contribution to water production in minerals. We investigated the detailed depth-dependent irradiation-induced substructures using TEM, STEM–EELS, and HSI–NMF analyses of the datasets obtained from a cross-sectional sample. The damage region was not amorphized, but it did exhibit characteristic spectroscopic features that strongly suggest chemical interactions of the implanted H with irradiation-induced defects in the alumina. Some of the H atoms were chemically trapped by broken O bonds caused by the energetic ion bombardment, resulting in formation of OH species. In addition, a high density of voids with diameters of around 1 nm was observed in the damaged region, particularly at a depth of ~100–300 nm. The observed nanocracks and exfoliated texture suggest that with increasing H-ion dose, the implanted H atoms became trapped and accumulate in the H-terminated nanospaces or clusters of vacancies to form nanobubbles, which develop into nanocracks and

eventually to exfoliation due to the coalescence of neighboring nanobubbles when the internal pressure increases beyond the fracture limit of alumina. Although most of the H_2 gas escaped through the leakage paths generated by the coalescence, a spectral feature implied a possibility that a small amount H_2 presumably remained in the nanovoids. We estimated the maximum concentration of the residual H_2 gas to be ~ 1 H/nm^3, or $\sim 0.5\%$ of the total implanted H in the region with the highest H concentration. On the other hand, the resulting fractures newly generate additional, highly reactive sites at which OH can be generated efficiently.

The present TEM and STEM–EELS results imply that solar-wind irradiation can contribute to the origin of water in the minerals on airless bodies. This hypothesis also implies that interstellar dust irradiated by H^+ due to supernova shocks probably has OH-bearing defects throughout the grains. The present experimental methodology—particularly using HVEM–STEM–EELS—can contribute further to the investigation of various experimental products in simulating space weathering, as well as of actual regolith grains brought back directly from airless bodies by spacecraft and/or presolar grains in primitive meteorites.

Declaration of Competing Interest

The authors declare that they have no known competing financial interests or personal relationships that could have appeared to influence the work reported in this paper.

APPENDIX A. SUPPLEMENTARY MATERIAL

Supplementary data to this article can be found online at https://doi.org/10.1016/j.gca.2021.09.031.

REFERENCES

Ahn C. C., Krivanek O. L. and Disko M. M. (1983) *EELS atlas: A Reference Collection of Electron Energy Loss Spectra Covering All Stable Elements.* HREM Facility, Center for Solid State Science, Arizona State University.

Arista N. R. (2000) Stopping of molecules and clusters. *Nucl. Instrum. Meth. B* **164**, 108–138.

Bandfield J. L., Poston M. J., Klima R. L. and Edwards C. S. (2018) Widespread distribution of OH/H_2O on the lunar surface inferred from spectral data. *Nat. Geosci.* **11**, 173–177.

Bonnet N., Brun N. and Colliex C. (1999) Extracting information from sequences of spatially resolved EELS spectra using multivariate statistical analysis. *Ultramicroscopy* **77**, 97–112.

Bosman M., Watanabe M., Alexander D. T. L. and Keast V. J. (2006) Mapping chemical and bonding information using multivariate analysis of electron energy-loss spectrum images. *Ultramicroscopy* **106**, 1024–1032.

Burgess K. D. and Stroud R. M. (2018) Phase-dependent space weathering effects and spectroscopic identification of retained helium in a lunar soil grain. *Geochim. Cosmochim. Acta* **224**, 64–79.

Bradley J. P. (2013) How and where did GEMS form? *Geochim. Cosmochim. Acta* **107**, 336–340.

Bradley J. P., Ishii H. A., Gillis-Davis J. J., Ciston J., Nielsen M. H., Bechtel H. A. and Martin M. C. (2014) Detection of solar wind-produced water in irradiated rims on silicate minerals. *Proc. Natl. Acad. Sci. U.S.A.* **111**, 1732–1735.

Bradley J. P. and Dai Z. R. (2004) Mechanism of formation of glass with embedded metal and sulfides. *Astrophys. J.* **617**, 650.

Burke D. J., Dukes C. A., Kim J. H., Shi J., Famá M. and Baragiola R. A. (2011) Solar wind contribution to surficial lunar water: Laboratory investigations. *Icarus* **211**, 1082–1088.

Carrez P., Demyk K., Cordier P., Gengembre L., Grimblot J., d'Hendecourt L., Jones A. P. and Leroux H. (2002) Low-energy helium ion irradiation-induced amorphization and chemical changes in olivine: Insights for silicate dust evolution in the interstellar medium. *Meteorit. Planet. Sci.* **37**, 1599–1614.

Christoffersen R., McKay D. S. and Keller L. P. (1996) Microstructure, chemistry, and origin of grain rims on ilmenite from the lunar soil finest fraction. *Meteorit. Planet. Sci.* **31**, 835–848.

Clark B. E., Hapke B., Pieters C. and Britt D. (2002) Asteroid space weathering and regolith evolution. In *Asteroids III* (eds. W. F. Bottke, A. Cellino, P. Paolicchi and R. P. Binzel). Univ. of Arizona Press, Tucson, AZ, pp. 255–271.

Clark R. N. (2009) Detection of adsorbed water and hydroxyl on the Moon. *Science* **326**, 562–564.

Day K. L. (1977) Irradiation of magnesium silicates with MeV protons. *Mon. Notices R. Astron. Soc.* **178**, 49–51.

Demyk K., Carrez P., Leroux H., Cordier P., Jones A. P., Borg J., Quirico E., Raynal P. I. and d'Hendecourt L. (2001) Structural and chemical alteration of crystalline olivine under low energy He^+ irradiation. *Astron. Astrophys.* **368**, L38–L41.

Demyk K., d'Hendecourt L., Leroux H., Jones A. P. and Borg J. (2004) IR spectroscopic study of olivine, enstatite and diopside irradiated with low energy H and He ions. *Astron. Astrophys.* **420**, 233–243.

Dran J. C., Durrieu L., Jouret C. and Maurette M. (1970) Habit and texture studies of lunar and meteoritic materials with a 1 MeV electron microscope. *Earth Planet. Sci. Lett.* **9**, 391–400.

Drude P. (1900) On the ionic theory of metals. *Phys. Z.* **1**, 161–165.

Egerton R. F. (1978) Formulae for light-element micro analysis by electron energy-loss spectrometry. *Ultramicroscopy* **3**, 243–251.

Fréchard S., Walls M., Kociak M., Chevalier J. P., Henry J. and Gorse D. (2009) Study by EELS of helium bubbles in a martensitic steel. *J. Nucl. Mater.* **393**, 102–107.

French R. H., Müllejans H. and Jones D. J. (1998) Optical properties of aluminum oxide: determined from vacuum ultraviolet and electron energy-loss spectroscopies. *J. Am. Ceram. Soc.* **81**, 2549–2557.

Goldstein B. E., Neugebauer M., Phillips J. L., Bame S., Gosling J. T. and McComas D. (1996) ULYSSES plasma parameters:

latitudinal, radial, and temporal variations. *Astron. Astrophys.* **316**, 296–303.

Hapke B. (2001) Space weathering from Mercury to the asteroid belt. *J. Geophys. Res.* **106**, 10039–10073.

Hatori S., Ishigami R., Kume K. and Suzuki K. (2021) Ion Accelerator Facility of the Wakasa Wan Energy Research Center for the Study of Irradiation Effects on Space Electronics. *Quantum Beam Sci.* **5**, 14.

Hatori S., Kurita T., Hayashi Y., Yamada M., Yamada H., Mori J., Hamachi H., Kimura S., Shimoda T., Hiroto M., Hashimoto T., Shimada M., Yamamoto H., Ohtani N., Yasuda K., Ishigami R., Sasase M., Ito Y., Hatashita M., Takagi K., Kume K., Fukuda S., Yokohama N., Kagiya G., Fukumoto S. and Kondo M. (2005) Developments and applications of accelerator system at the Wakasa Wan Energy Research Center. *Nucl. Instrum. Meth. B* **241**, 862–869.

Harries D. and Langenhorst F. (2014) The mineralogy and space weathering of a regolith grain from 25143 Itokawa and the possibility of annealed solar wind damage. *Earth Planets Space* **66**, 1–11.

Heber V. S., Baur H., Bochsler P., McKeegan K. D., Neugebauer M., Reisenfeld D. B., Wieler R. and Wiens R. C. (2012) Isotopic mass fractionation of solar wind: evidence from fast and slow solar wind collected by the Genesis mission. *Astrophys. J.* **759**, 121–133.

Hobbs L. W. (1994) Topology and geometry in the irradiation-induced amorphization of insulators. *Nucl. Instrum. Meth. B* **91**, 30–42.

Hobbs L. W., Clinard, Jr., F. W., Zinkle S. J. and Ewing R. C. (1994) Radiation effects in ceramics. *J. Nucl. Mater.* **216**, 291–321.

Hobbs L. W. and Pascucci M. R. (1980) Radiolysis and defect structure in electron-irradiated α-quartz. *J. Phys. Colloq.* **41**, C6-237–242.

Hutcheon I. D., Huss G. R., Fahey A. J. and Wasserburg G. J. (1994) Extreme ^{26}Mg and ^{17}O enrichments in an Orgueil corundum: Identification of a presolar oxide grain. *Astrophys. J. Lett.* **425**, L97–L100.

Ichimura A. S., Zent A. P., Quinn R. C., Sanchez M. R. and Taylor L. A. (2012) Hydroxyl (OH) production on airless planetary bodies: Evidence from H^+/D^+ ion-beam experiments. *Earth Planet. Sci. Lett.* **345**, 90–94.

Ishino S. (1993) Time and temperature dependence of cascade induced defect production in in situ experiments and computer simulation. *J. Nucl. Mater.* **206**, 139–155.

Jäger C., Fabian D., Schrempel F., Dorschner J., Henning T. and Wesch W. (2003) Structural processing of enstatite by ion bombardment. *Astron. Astrophys.* **401**, 57–65.

Jiang N. and Spence J. C. (2011) *In situ* EELS study of dehydration of Al(OH)$_3$ by electron beam irradiation. *Ultramicroscopy* **111**, 860–864.

Jones A. P., Tielens A. G. G. M. and Hollenbach D. J. (1996) Grain shattering in shocks: The interstellar grain size distribution. *Astrophys. J.* **469**, 740.

Keller L. P. and McKay D. S. (1997) The nature and origin of rims on lunar soil grains. *Geochim. Cosmochim. Acta* **61**, 2331–2341.

Kemper F., Vriend W. J. and Tielens A. G. G. M. (2004) The absence of crystalline silicates in the diffuse interstellar medium. *Astrophys. J.* **609**, 826–837.

Kemper F., Vriend W. J. and Tielens A. G. G. M. (2005) Erratum: "The absence of crystalline silicates in the diffuse interstellar medium" (ApJ, 609, 826 [2004]). *Astrophys. J.* **633**, 534–534.

Leapman R. D. and Sun S. (1995) Cryo-electron energy loss spectroscopy: observations on vitrified hydrated specimens and radiation damage. *Ultramicroscopy* **59**, 71–79.

Li S. and Milliken R. E. (2017) Water on the surface of the Moon as seen by the Moon Mineralogy Mapper: Distribution, abundance, and origins. *Sci. Adv.* **3**, e1701471.

Li S., Lucey P. G., Milliken R. E., Hayne P. O., Fisher E., Williams J. P., Hurley D. M. and Elphic R. C. (2018) Direct evidence of surface exposed water ice in the lunar polar regions. *Proc. Natl. Acad. Sci. U.S.A.* **115**, 8907–8912.

Managadze G. G., Cherepin V. T., Shkuratov Y. G., Kolesnik V. N. and Chumikov A. E. (2011) Simulating OH/H$_2$O formation by solar wind at the lunar surface. *Icarus* **215**, 449–451.

Matsumoto T., Tsuchiyama A., Miyake A., Noguchi T., Nakamura M., Uesugi K., Takeuchi A., Suzuki Y. and Nakano T. (2015) Surface and internal structures of a space-weathered rim of an Itokawa regolith particle. *Icarus* **257**, 230–238.

Matsumoto T., Tsuchiyama A., Uesugi K., Nakano T., Uesugi M., Matsuno J., Naganoe T., Shimada A., Takeuchi A., Suzuki Y., Nakamura T., Nakamura M., Gucsik A., Nagaki K., Sakaiya T. and Kondo T. (2016) Nanomorphology of Itokawa regolith particles: application to space-weathering processes affecting the Itokawa asteroid. *Geochim. Cosmochim. Acta* **187**, 195–217.

Muto S. and Tatsumi K. (2017) Detection of local chemical states of lithium and their spatial mapping by scanning transmission electron microscopy, electron energy-loss spectroscopy and hyperspectral image analysis. *Microscopy* **66**, 39–49.

Muto S., Tatsumi K., Ikeda K. and Orimo S. (2009) Dehydriding process of α-AlH$_3$ observed by transmission electron microscopy and electron energy-loss spectroscopy. *J. Appl. Phys.* **105** 123514.

Muto S. and Shiga M. (2020) Application of machine learning techniques to electron microscopic/spectroscopic image data analysis. *Microscopy* **69**, 110–122.

Nakauchi Y., Abe M., Ohtake M., Matsumoto T., Tsuchiyama A., Kitazato K., Yasuda K., Suzuki K. and Nakata Y. (2021) The formation of H$_2$O and Si-OH by H$_2^+$ irradiation in major minerals of carbonaceous chondrites. *Icarus* **355**, 114140.

Nittler L. R., Alexander C. M. D., Gao X., Walker R. M. and Zinner E. (1997) Stellar sapphires: The properties and origins of presolar Al$_2$O$_3$ in meteorites. *Astrophys. J.* **483**, 475.

Nittler L. R., Alexander C. M. D., Gallino R., Hoppe P., Nguyen A. N., Stadermann F. J. and Zinner E. K. (2008) Aluminum-, calcium-and titanium-rich oxide stardust in ordinary chondrite meteorites. *Astrophys. J.* **682**, 1450.

Noguchi T., Nakamura T., Kimura M., Zolensky M. E., Tanaka M., Hashimoto T., Konno M., Nakato A., Ogami T., Fujimura A., Abe M., Yada T., Mukai T., Ueno M., Okada T., Shirai K., Ishibashi Y. and Okazaki R. (2011) Incipient space weathering observed on the surface of Itokawa dust particles. *Science* **333**, 1121–1125.

Noguchi T., Kimura M., Hashimoto T., Konno M., Nakamura T., Zolensky M. E., Okazaki R., Tanaka M., Tsuchiyama A., Nakato A., Ogami T., Ishida H., Sagae R., Tsujimoto S., Matsumoto T., Matsuno J., Fujimura A., Abe M., Yada T., Mukai T., Ueno M., Okada T., Shirai K. and Ishibashi Y. (2014) Space weathered rims found on the surfaces of the Itokawa dust particles. *Meteorit. Planet. Sci.* **49**, 188–214.

Ono K., Miyamoto M., Kurata H., Haruta M. and Yatomi A. (2019) Dynamic behavior of helium bubbles at high temperature in Si studied by in situ TEM, STEM-EELS, and TDS. *J. Appl. Phys.* **126** 135104.

Pells G. P. (1994) Radiation damage effects in alumina. *J. Am. Ceram. Soc.* **77**, 368–377.

Perevalov T. V., Gritsenko V. A. and Kaichev V. V. (2010) Electronic structure of aluminum oxide: ab initio simulations of α and γ phases and comparison with experiment for amorphous films. *EPJ Appl. Phys.* **52**, 30501.

Pieters C. M. and Noble S. K. (2016) Space weathering on airless bodies. *J. Geophys. Res. Planet.* **121**, 1865–1884.

Pieters C. M., Taylor L. A., Noble S. K., Keller L. P., Hapke B., Morris R. V., Allen C. C., McKAY D. S. and Wentworth S. (2000) Space weathering on airless bodies: Resolving a mystery with lunar samples. *Meteorit. Planet. Sci.* **35**, 1101–1107.

Pieters C. M., Goswami J. N., Clark R. N., Annadurai M., Boardman J., Buratti B., Combe J.-P., Dyar M. D., Green R., Head J. W., Hibbitts C., Hicks M., Isaacson P., Klima R., Kramer G., Kumar S., Livo E., Lundeen S., Malaret E., McCord T., Mustard J., Nettles J., Petro N., Runyon C., Staid M., Sunshine J., Taylor L. A., Tompkins S. and Varanasi P. (2009) Character and spatial distribution of OH/H_2O on the surface of the Moon seen by M^3 on Chandrayaan-1. *Science* **326**, 568–572.

Reisenfeld D. B., Steinberg J. T., Barraclough B. L., Dors E. E., Wiens R. C., Neugebauer M., Reinard A. and Zurbuchen T. (2003) Comparison of the Genesis solarwind regime algorithm results with solarwind composition observed by ACE. *AIP Conf. Proc.* **679**, 632–635.

Reisenfeld D. B., Burnett D. S., Becker R. H., Grimberg A. G., Heber V. S., Hohenberg C. M., Jurewicz A. J. G., Meshik A., Pepin R. O., Raines J. M., Schlutter D. J., Wieler R., Wiens R. C. and Zurbuchen T. H. (2007) Elemental abundances of the bulk solar wind: analyses from Genesis and ACE. *Space Sci. Rev.* **130**, 79–86.

Rife J. C., Donnelly S. E., Lucas A. A., Gilles J. M. and Ritsko J. J. (1981) Optical absorption and electron-energy-loss spectra of helium microbubbles in aluminum. *Phys. Rev. Lett.* **46**, 1220.

Sasajima N., Matsui T., Furuno S., Hojou K. and Otsu H. (1999) Damage accumulation in Al_2O_3 during H_2^+ or He^+ ion irradiation. *Nucl. Instrum. Meth. B* **148**, 745–751.

Sigmund P., Bitensky I. S. and Jensen J. (1996) Molecule and cluster bombardment: Energy loss, trajectories, and collision cascades. *Nucl. Instrum. Meth. B* **112**, 1–11.

Sunshine J. M., Farnham T. L., Feaga L. M., Groussin O., Merlin F., Milliken R. E. and A'Hearn M. F. (2009) Temporal and spatial variability of lunar hydration as observed by the Deep Impact spacecraft. *Science* **326**, 565–568.

Takigawa A., Tachibana S., Huss G. R., Nagashima K., Makide K., Krot A. N. and Nagahara H. (2014) Morphology and crystal structures of solar and presolar Al_2O_3 in unequilibrated ordinary chondrites. *Geochim. Cosmochim. Acta* **124**, 309–327.

Takigawa A., Stroud R. M., Nittler L. R., Alexander C. M. D. and Miyake A. (2018) High-temperature dust condensation around an AGB star: Evidence from a highly pristine presolar corundum. *Astrophys. J. Lett.* **862**, L13.

Taverna D., Kociak M., Stéphan O., Fabre A., Finot E., Décamps B. and Colliex C. (2008) Probing physical properties of confined fluids within individual nanobubbles. *Phys. Rev. Lett.* **100** 035301.

Thompson M. S., Christoffersen R., Zega T. J. and Keller L. P. (2014) Microchemical and structural evidence for space weathering in soils from asteroid Itokawa. *Earth Planets Space* **66**, 1–10.

Trebbia P. and Bonnet N. (1990) EELS elemental mapping with unconventional methods I. Theoretical basis: Image analysis with multivariate statistics and entropy concepts. *Ultramicroscopy* **34**, 165–178.

Vidali G. (2013) H_2 formation on interstellar grains. *Chem. Rev.* **113**, 8762–8782.

Walsh C. A., Yuan J. and Brown L. M. (2000) A procedure for measuring the helium density and pressure in nanometre-sized bubbles in irradiated materials using electron-energy-loss spectroscopy. *Philos. Mag. A* **80**, 1507–1543.

White C. W., McHargue C., Sklad P. S., Boatner L. A. and Farlow G. C. (1989) Ion implantation and annealing of crystalline oxides. *Mater. Sci. Rep.* **4**, 41–146.

Wieser M., Wurz P., Brüning K. and Heiland W. (2002) Scattering of atoms and molecules off a magnesium oxide surface. *Nucl. Instrum. Meth. B* **192**, 370–380.

Zeidler S., Posch T. and Mutschke H. (2013) Optical constants of refractory oxides at high temperatures-Mid-infrared properties of corundum, spinel, and α-quartz, potential carriers of the 13 μm feature. *Astron. Astrophys.* **553**, A81.

Zeller E. J., Ronca L. B. and Levy P. W. (1966) Proton-induced hydroxyl formation on the lunar surface. *J. Geophys. Res.* **71**, 4855–4860.

Ziegler J. F., Biersak J. P. and Littmark U. (1985) *The Stopping and Range of Ions in Solids*. Pergamon Press, New York.

Ziegler J. F., Biersack J. P. and Ziegler M. D. (2013) *The Stopping and Range of Ions in Matter*. SRIM http://www.srim.org.

Zinkle S. J. and Kinoshita C. (1997) Defect production in ceramics. *J. Nucl. Mater.* **251**, 200–217.

Zinkle S. J. (2012) Effect of H and He irradiation on cavity formation and blistering in ceramics. *Nucl. Instrum. Meth. B* **286**, 4–19.

Zhu C., Crandall P. B., Gillis-Davis J. J., Ishii H. A., Bradley J. P., Corley L. M. and Kaiser R. I. (2019) Untangling the formation and liberation of water in the lunar regolith. *Proc. Natl. Acad. Sci. U.S.A.* **116**, 11165–11170.

Associate editor: Hope Ishii